Anisotropic thermoelectric properties of $Bi_{1.9}Lu_{0.1}Te_{2.7}Se_{0.3}$ textured via spark plasma sintering

Alexei Vasil'ev[a], Maxim Yaprintsev[a], Oleg Ivanov[a,*], Elena Danshina[b]

[a] Belgorod State University, Pobedy 85, 394015, Russian Federation
[b] Belgorod State Technological University Named After V.G. Shukhov, Belgorod, 308012, Russian Federation

ARTICLE INFO

ABSTRACT

Spark plasma sintering method was applied to prepare bulk *n*-type $Bi_{1.9}Lu_{0.1}Te_{2.7}Se_{0.3}$ samples highly textured along the 001 direction parallel to the pressing direction. The texture development is confirmed by X-ray diffraction analysis and scanning electron microscopy. The grains in the textured samples form ordered lamellar structure and lamellar sheets lie in plane perpendicular to the pressing direction. The average grain size measured along the pressing direction is much less as compared to the average grain size measured in the perpendicular direction (~ 50 nm against ~ 400 nm). A strong anisotropy in the transport properties measured along directions parallel and perpendicular to the pressing direction within the $290 \div 650$ K interval was found. The specific electrical resistivity increases and the thermal conductivity decreases for the parallel orientation as compared to these properties for the perpendicular orientation. The Seebeck coefficient for both orientations is almost equal. Increase of the electrical resistivity is stronger than decrease of the thermal conductivity resulting in almost three-fold enhancement of the thermoelectric figure-of-merit coefficient for the perpendicular orientation (~ 0.68 against ~ 0.24 at ~ 420 K). The texturing effect can be attributed to (i) recovery of crystal structure anisotropy typical for the single crystal Bi_2Te_3-based alloys and (ii) grain boundary scattering of electrons and phonons. An onset of intrinsic conductivity observed above $T_d \approx 410$ K results in appearance of maxima in the temperature dependences of the specific electrical resistivity, the Seebeck coefficient and the thermoelectric figure-of-merit coefficient and minimum in the temperature dependence of the total thermal conductivity. The intrinsic conductivity is harmful for the thermoelectric efficiency enhancement since thermal excitation of the electron-hole pairs reduces the Seebeck coefficient and increases the thermal conductivity.

1. Introduction

Currently, bismuth telluride, Bi_2Te_3, and *n*- and *p*-type Bi_2Te_3-based alloys, are known to be the best thermoelectric materials for near room temperature applications [1,2]. For instance, *n*-type thermoelectrics are the $Bi_2Te_{3-x}Se_x$ solid solutions with optimal composition corresponding to $x = 0.3$ [3,4]. One of specific characteristics of these materials remarkably effecting on their thermoelectric properties is a high enough anisotropy in the transport properties like the electrical conductivity and the thermal conductivity [5,6]. The matter is Bi_2Te_3-based alloys have space $R\bar{3}m$ symmetry and unit cell parameters measured along the rhombohedral *c*-axis (the *c* parameter) or within the *a-b* plane oriented perpendicular to the *c*-axis (the *a* and *b* parameters) are very different from each other. For instance, the room temperature parameters for Bi_2Te_3 are $c = 30.487$ Å and $a = b = 4.384$ Å. In turn, a big difference in the *c* and $a = b$ parameters is originated from crystal structure

anisotropy due to mainly combination of various types of bonding between atoms. Actually, the Bi_2Te_3 crystal structure consists of 15 layers stacked along the *c*-axis and presents the combination of three hexagonal layer stacks of the composition in which each set consists of five atoms (Te_1–Bi–Te_2–Bi–Te_1) [7]. The bonding within the Te_1–Bi–Te_2–Bi–Te_1 layer is assumed to be covalent, while the Te_1–Te_1 layers are bonded by the van der Waals forces. Naturally, the physical properties measured parallel or perpendicular to the layers happen different. Anisotropy in the specific electrical resistivity, ρ, and the thermal conductivity, k, of the Bi_2Te_3 and Bi_2Te_3-based single crystals are often characterized by the ρ_c/ρ_{ab} and k_c/k_{ab} coefficients, where the *c* and *ab* subscripts correspond to the directions perpendicular or parallel to the layers, respectively. For Bi_2Te_3, anisotropy in the transport properties is described as $\rho_c/\rho_{ab} \approx 5 \div 5.5$ depending on type and concentration of the charge carriers, and $k_c/k_{ab} \approx 2$ [7–9]. In contrast to k and ρ, the Seebeck coefficient, S, is far less anisotropic quantity.
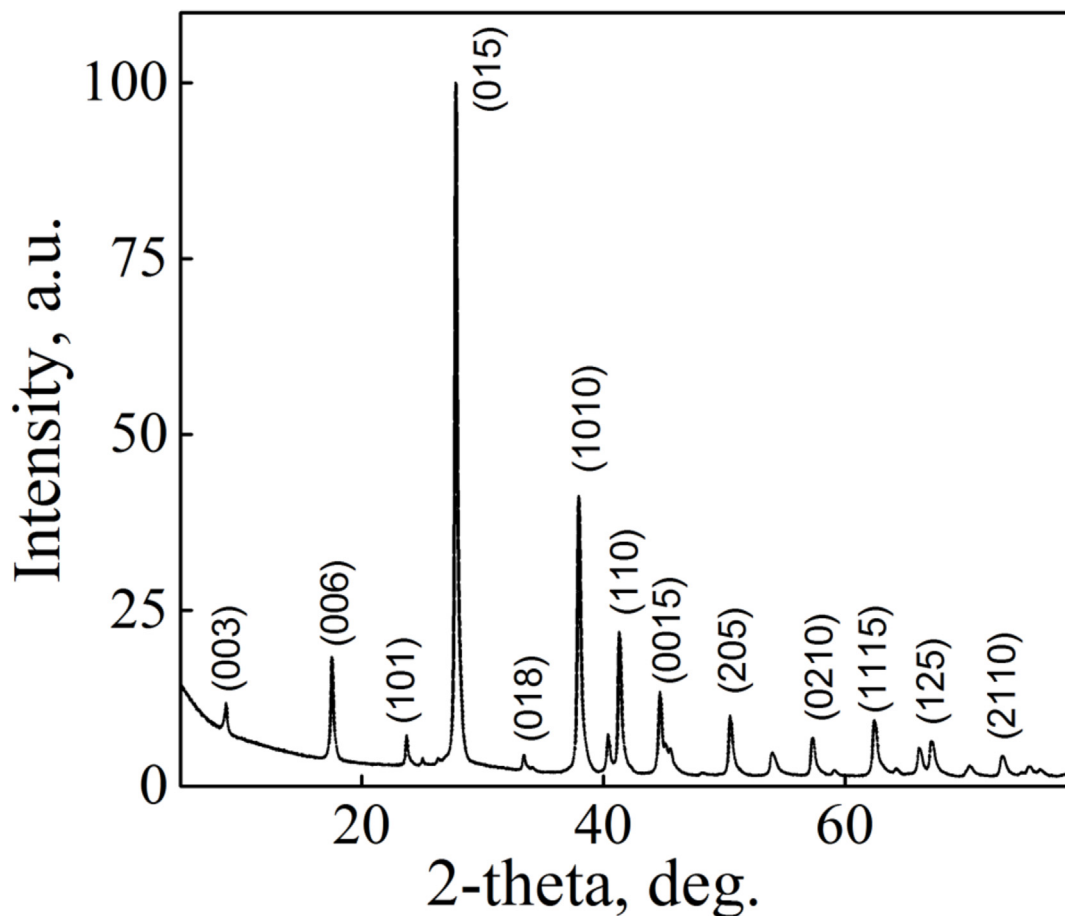

Fig. 1. XRD pattern for the starting powder.

As is known [8], thermoelectric efficiency of materials can be estimated by the dimensionless figure-of-merit coefficient, ZT, expressed as $(S^2/\rho k)T$, where T is the absolute temperature. Since for the Bi_2Te_3 single crystals ρ and k are highly anisotropic, ZT is anisotropic, too. For grained material with completely random orientation of the grains, the thermoelectric figure-of-merit coefficient is already isotropic. To recovery, at least, partially, the anisotropy in the transport properties of the grained materials based on Bi_2Te_3, microstructure texturing is often and fruitfully applied [8–16]. At the texturing, a preferential orientation of the grains can be yielded and some physical properties measured along the texturing direction or within the plane parallel to this direction start to be different again. There are a few technological ways to texture Bi_2Te_3 and Bi_2Te_3-based alloys like extrusion, hot pressing, spark plasma sintering. It should be noted, besides recovery of the anisotropy due to difference in properties measured along the *c*-axis or within the *a-b* plane, the texturing can result in an additional anisotropy developing via ordering of the grains. Indeed, if the grains have the sizes different enough in various directions, then the preferential grain orientation in the texturing direction can lead to appearance of difference in intergrain spacing measured parallel and perpendicular to the texturing axis. In this case, contribution of the grain boundaries to the electrical and thermal properties can be also different for these two directions.

The aim of this paper is to analyze the texturing effect on the thermoelectric properties of *n*-type $Bi_{1.9}Lu_{0.1}Te_{2.7}Se_{0.3}$. The composition under study contents a small amount of Lu. It is known that the thermoelectric efficiency of Bi_2Te_3 and Bi_2Te_3-based alloys can be remarkably enhanced via rare earth element doping [17–20]. However, here we will not discuss the Lu effect on the thermoelectric properties of $Bi_{1.9}Lu_{0.1}Te_{2.7}Se_{0.3}$. Results of this effect study will be published

elsewhere later. Only the texturing effect will be under detailed examination.

2. Materials and methods

Analytically pure chemicals (Bi_2O_3, TeO_2, SeO_2 and $Lu(CH_3COO)_3$) taken as precursors were weighed according to the stoichiometric $Bi_{1.9}Lu_{0.1}Te_{2.7}Se_{0.3}$ composition. These precursors together with 20 g NaOH as the pH-controller were put into conical flask equipped with condenser and magnetic stirrer and filled with about 500 mL ethylene glycol, acting as the solvent and reductant. Then, the solution was heated up to 373K and maintained for a few hours to get a transparent solution. After, the system was maintained at 458 K for 24 h to complete the reaction. Finally, the system was cooled down to room temperature and synthesized black precipitate was washed with water and isopropanol to remove NaOH and by-products and dried in vacuum at 373 K.

Spark plasma sintering (SPS) method by using a SPS-25/10 system was applied to compact the synthesized powder at pressure of 40 MPa, temperature of 780 K and sintering time of 5 min, resulting in the cylinders of Ø20 mm × 15 mm. The bars of 2 × 2 × 10 mm and the disks of Ø10 × 2 mm were cut along in-plane and out of plane directions of these cylinders.

A density of the sample studied was measured by the Archimedes' method.

X-ray diffraction (XRD) analysis was performed by a Rigaku Ultima IV diffractometer with CuK_α - radiation to determine the phase composition of the starting powder and the bulk sample.

To determine the correct elemental composition of material prepared, a Shimadzu ICP (Inductively Coupled Plasma) emission

spectrometer ICPE-9000 was applied.

To observe the starting powder morphology and estimate the particles size, a model JEM - 2100 transmission electron microscope (TEM) was used.

Scanning electron microscope (SEM), a Nova NanoSEM 450, was also applied to study the microstructure features of the bulk samples.

The specific electrical resistivity and the Seebeck coefficient of the sample bars were measured by using a ZEM-3 system. The type, concentration, n, and Hall mobility, μ_H, of the majority charge carriers for the same samples were extracted from the Hall Effect study carried out by a Mini Cryogen Free Measurements System (Cryogenic Ltd, UK).

A TC-1200 system was applied to determine the thermal conductivity of the disk-shaped samples by the laser flash method.

3. Results and discussion

3.1. The textured structure characterization

The XRD pattern for the starting $Bi_{1.9}Lu_{0.1}Te_{2.7}Se_{0.3}$ powder taken at room temperature is shown in Fig. 1. According to the XRD analysis, this powder is single hexagonal phase characteristic for pure $Bi_2Te_{2.7}Se_{0.3}$ (PDF#50-0954). All the diffraction peaks can be exactly indexed with the standard diffraction planes corresponding to space symmetry $R\overline{3}m$ group.

The starting powder mainly consists of hexagonal nanoplates as is shown in the TEM image in Fig. 2. The formation of the hexagonal nanoplates can be related to their anisotropic structure.

To determine an average nanoplates size, the histogram of nanoplates size distribution was plotted (Fig. 3).

This histogram can be described by a lognormal unimodal distribution. The lognormal probability density function can be expressed as [21].

$$P(d) = \frac{1}{\sqrt{2\pi}\sigma d}\exp\left(-\frac{(\ln d - \ln\overline{d})^2}{2\sigma^2}\right),$$ (1)

where d is the nanoplates size, $\overline{d}$ is the average nanoplate size and σ is the standard deviation of the logarithms of the nanoplates sizes. The standard deviation is measure of the width of the distribution. The $\overline{d}$ size corresponds to maxima on the fitting curve in Fig. 3. One can see that expression (1) reproduces the experimental nanoplate size distribution very well. By fitting this distribution, the values of $\overline{d}$ and σ were estimated as ∼285 nm and ∼0.32, respectively.

To prepare the bulk samples suitable to examine the thermoelectric properties, the synthesized $Bi_{1.9}Lu_{0.1}Te_{2.7}Se_{0.3}$ powder was further compacted by spark plasma sintering method. The density of the bulk samples was equal to 7.4 g/cm^3, which is ∼95% of the theoretical density of (7.78 g/cm^3, according to Ref. [18]).

Content of Lu and Se in the bulk samples was determined by the ICP emission spectrometer. Since both wastage and volatilization of some elements are unavoidable during spark plasma sintering, the real composition of the SPS-prepared material may deviate from the nominal one. However, according to analysis results, content of Lu and Se was equal to 2.19 and 6.09 at. %, respectively, that is in well agreement with the $Bi_{1.9}Lu_{0.1}Te_{2.7}Se_{0.3}$ composition.

It was found that the bulk $Bi_{1.9}Lu_{0.1}Te_{2.7}Se_{0.3}$ samples are highly textured. First of all, this texturing results in a big difference in the XRD patterns collected on surfaces perpendicular (Fig. 4 (a)) and parallel (Fig. 4 (b)) to the applied SPS pressure. Although all the peaks can be assigned to rhombohedral $R\overline{3}m$ structure with $c = 30.355$ Å and $a = b = 4.354$ Å, that is positions of these peaks are independent on the pressing direction, the intensities of some peaks are strongly dependent on this direction. A clear enhancement in the intensity for the (00l)
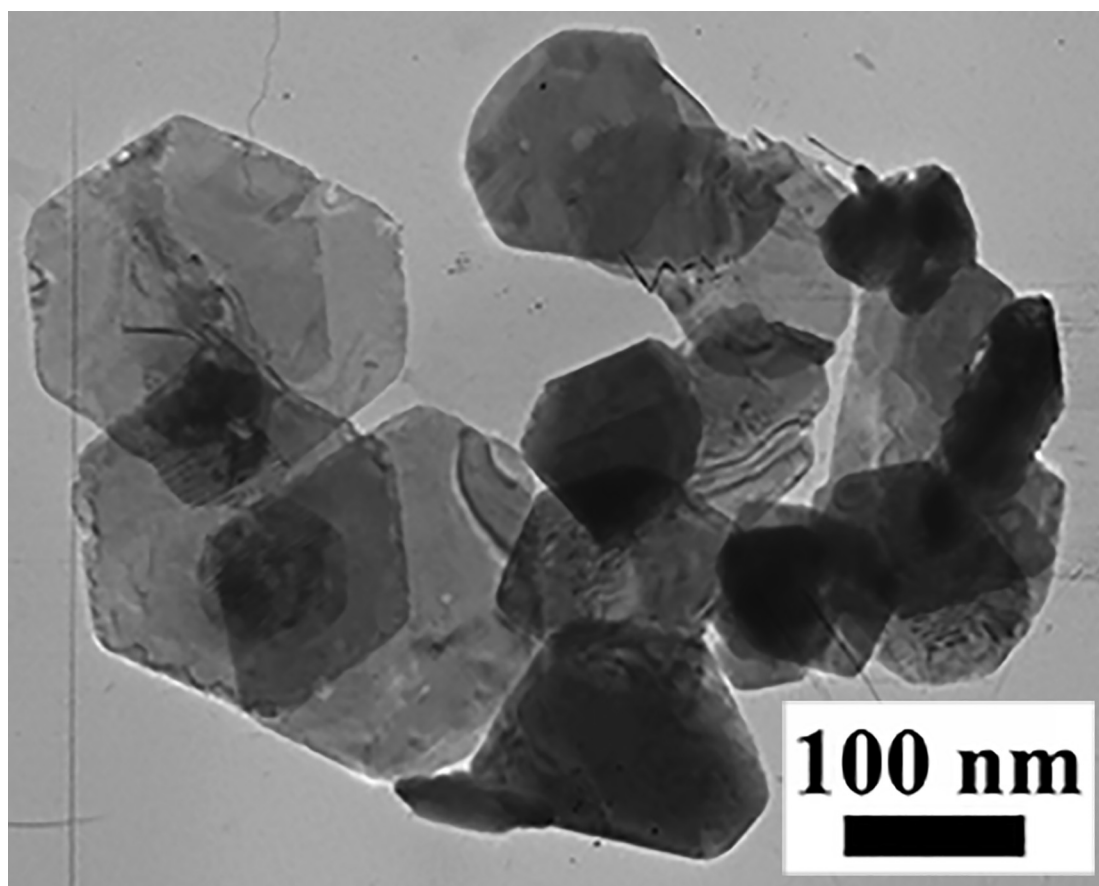

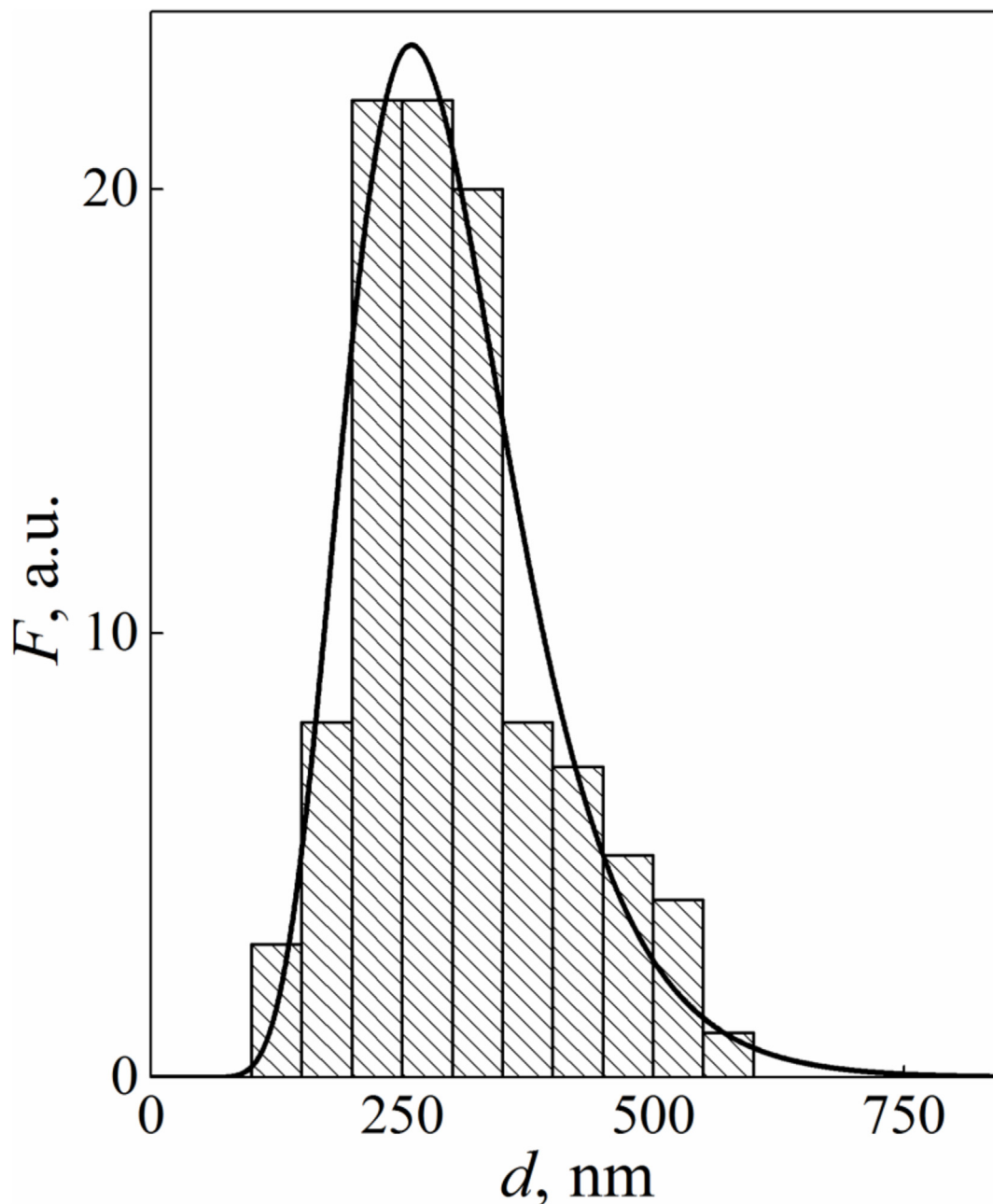Fig. 2. TEM image of the hexagonal nanoparticles.

Fig. 3. Histogram of the nanoplate size distribution for the starting powder. Solid line is the fitting curve corresponding to the lognormal unimodal distribution.

peaks is observed in the XRD pattern taken for surface oriented perpendicular to the pressing direction (Fig. 4 (a)). In turn, the intensity of the (11*l*) peaks also increases in the XRD pattern taken for other pressing direction (Fig. 4 (b)). Such redistribution in the intensity of peaks can be related to a lamellar texture formation with preferential orientation of the grains in the pressing direction. It should be noted that the XRD pattern taken for the powder prepared by grinding the textured sample (Fig. 4 (c)) already corresponds to the XRD pattern characteristic for the starting $Bi_{1.9}Lu_{0.1}Te_{2.7}Se_{0.3}$ powder (Fig. 1), that is redistribution in the intensity of the (00*l*) and (11*l*) peaks specific for textured anisotropic samples naturally vanishes in the isotropic powder.

The schematic of the texturing found in the sample studied is shown in Fig. 5. To plot this schematic, each grain was presented as an ellipsoid. So, in the plane parallel to the pressing direction, the grain is imaged as an ellipse. In turn, these grains preferentially lie in the planes.

Perpendicular to the pressing direction as shown in the left in Fig. 5.

The orientation of the *c*-axis and the *a-b* plane in the grain is shown in the right in Fig. 5. Thus, in the textured sample the *c*-axes of the grains are preferentially directed parallel to the pressing direction, while the *a-b* planes of the grains are preferentially oriented perpendicular to the pressing direction.

The degree of preferential grain orientation for the textured $Bi_{1.9}Lu_{0.1}Te_{2.7}Se_{0.3}$ sample can be estimated in terms of the orientation factor, *f*, given by Refs. [11,12].

$$f = \frac{p - p_0}{1 - p_0},$$

(2)

with *p* and p_0 defined as

$$p = \frac{I(00l)}{\sum I(hkl)}, \text{ and } p_0 = \frac{I_0(00l)}{\sum I_0(hkl)},$$

(3)

where the intensities *I* and I_0 are corresponding to oriented (textured) and non-oriented (non-textured) samples, respectively. Ideally, $f = 1$ is

(caption on next page)
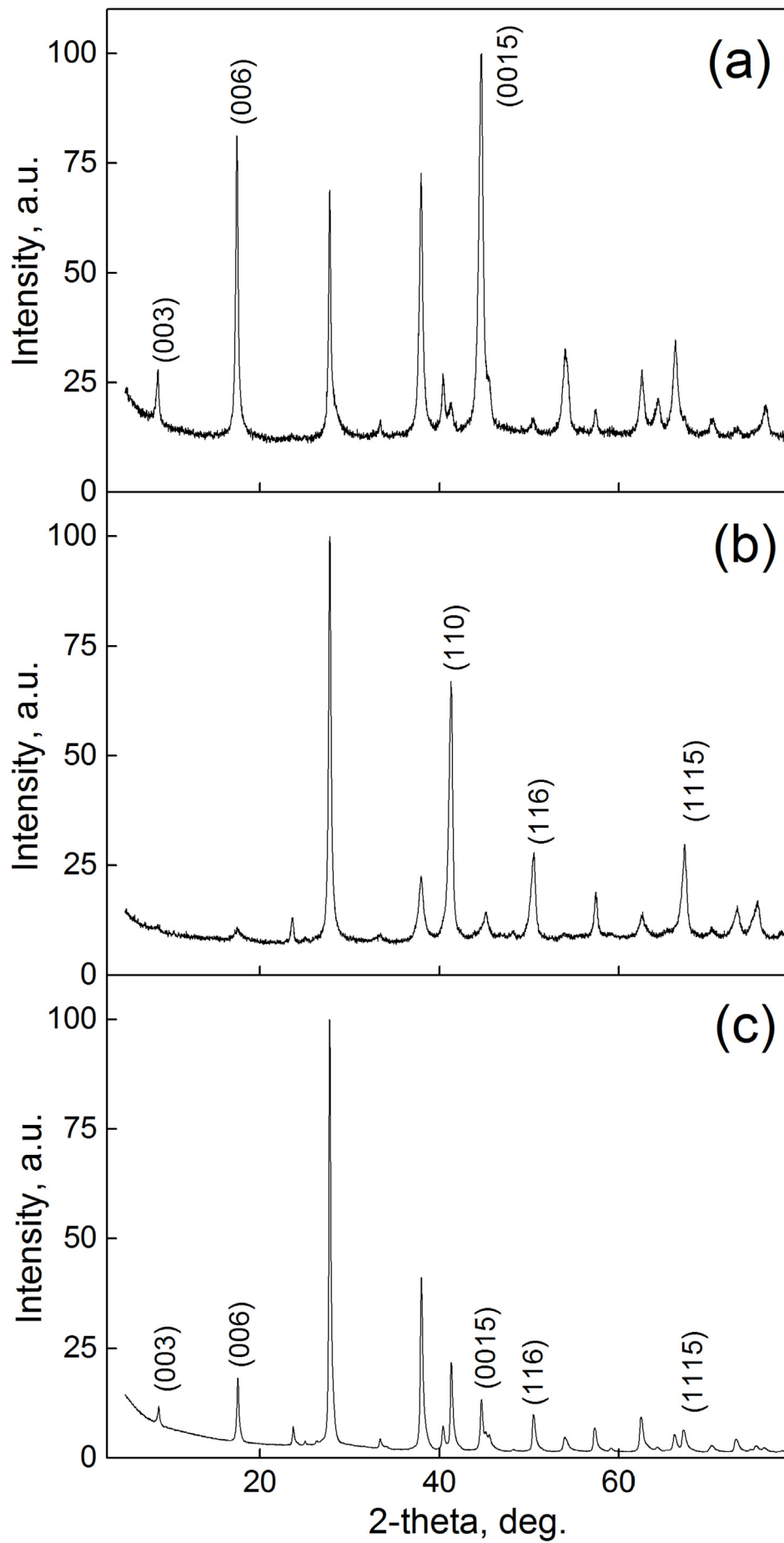
Fig. 4. XRD patterns for the bulk sample taken on the surfaces perpendicular (a) and parallel (b) to the pressing direction, and for the powder prepared by grinding the textured sample (c).

for completely oriented (like single crystal) and $f = 0$ is for completely non-oriented samples (powder or the grained material with completely random grain orientation).

To estimate the f factor for the sample studied, the XRD patterns in Fig. 4 (a) and Fig. 4 (c) were used to calculate the p and p_0 values. The result yields $f \approx 0.38$. Thus, it is concluded that the $Bi_{1.9}Lu_{0.1}Te_{2.7}Se_{0.3}$ samples highly oriented along c-axis were really prepared by SPS in our experiment.

Fig. 6 shows the SEM-images of the grain structures recorded on the fractured surfaces oriented parallel (a) and perpendicular (b) to the pressing direction.
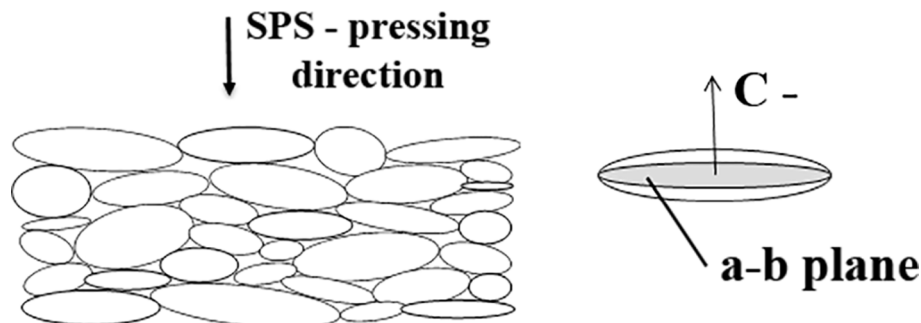
Disordered grain structure with the grains of $\leq 1\,\mu m$ and having mainly irregular shape can be found in Fig. 6 (a). In contrast to Fig. 6 (a), the grains in Fig. 6 (b) form ordered lamellar structure and lamellar sheets lie in plane perpendicular to the pressing direction. Such kind of grain alignment resulting in enhanced lamination has to release the strain created by the high uniaxial pressure applied during the SPS process. So, the SEM images in Fig. 6 are consistent with the XRD results.

The lamellar sheets in Fig. 6 (b) consist of the grains elongated in plane perpendicular to the pressing direction, that is the grain sizes in the direction parallel and perpendicular to the pressing direction are rather different. To estimate the average grain size, $\overline{D}$, in both directions, the histograms of the grain size distribution were plotted (Fig. 7). The sizes, D, of more than 100 grains were measured on the SEM images to obtain the reliable size distribution. The grain size distributions were discretized by dividing them into the 100- and 10 nm - width segments for parallel (Fig. 6 (a)) and perpendicular (Fig. 6 (b)) orientations, respectively.
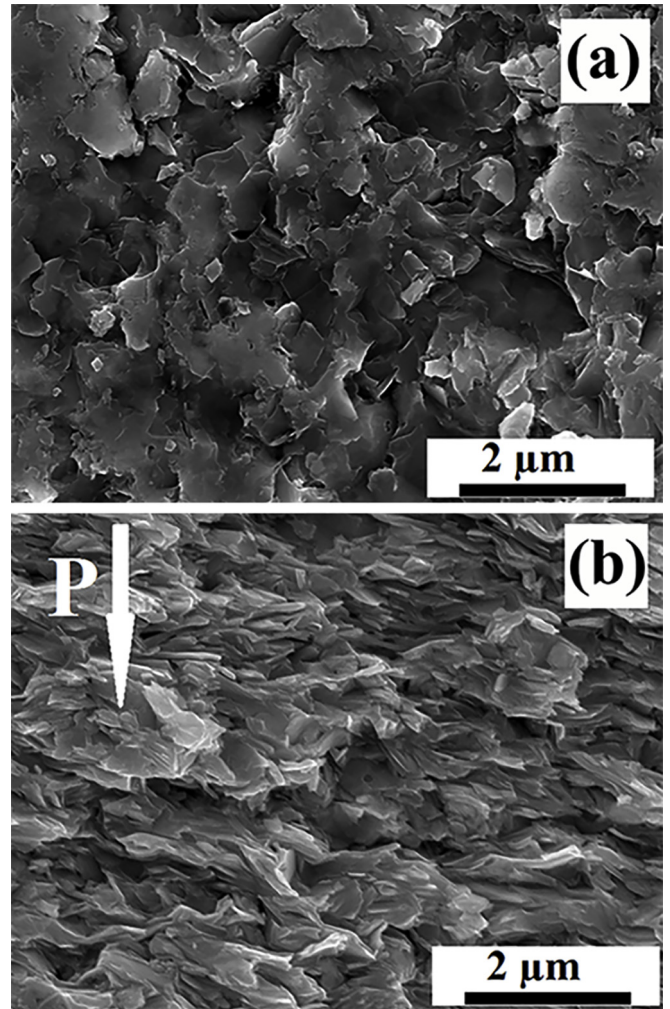
The lognormal unimodal distribution corresponding to expression (1) can be again applied to fit the experimental histograms in Fig. 7. The $\overline{D}$ and σ values were estimated as $\sim 400\,nm$ and $\sim 50\,nm$, and ~ 0.47 and ~ 0.27, for directions parallel and perpendicular to the pressing direction, respectively. So, the average grain size measured along the pressing direction (or along the c-axis) is much less as compared to the average grain size measured in other direction (within the a-b plane). Besides, the grain size distribution in the first case is narrower as the standard deviation is also less (~ 0.27 against ~ 0.47).

3.2. The texturing effect on the specific electrical resistivity

Let us now discuss the texturing effect on the thermoelectric properties of the bulk $Bi_{1.9}Lu_{0.1}Te_{2.7}Se_{0.3}$ sample. These properties including the specific electrical resistivity, the Seebeck coefficient and the thermal conductivity were measured along both directions. First of them corresponds to the direction parallel to the pressing direction (parallel orientation), and the second direction is perpendicular to the pressing direction (perpendicular orientation).

Fig. 6. SEM images taken on the fractured surfaces perpendicular (a) and parallel (b) to the pressing direction. The pressing direction is indicated by arrow in Fig. (b).

The $\rho(T)$ dependences measured for the parallel and perpendicular orientations are presented in Fig. 8.

First of all, one can see that the electrical resistivity for the parallel orientation is much more as compared to that for the perpendicular orientation within whole temperature range under study. However, although the $\rho(T)$ changes are more pronounced for the parallel orientation, the $\rho(T)$ behavior for both orientations are quantity similar.
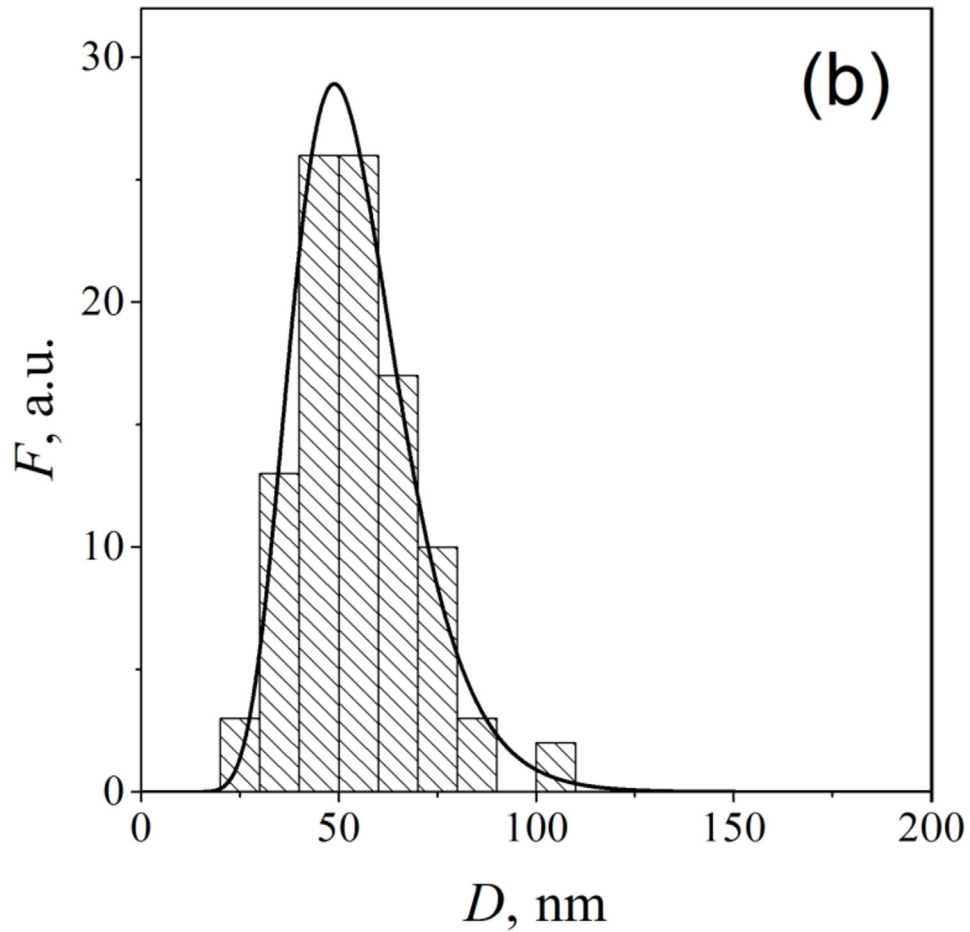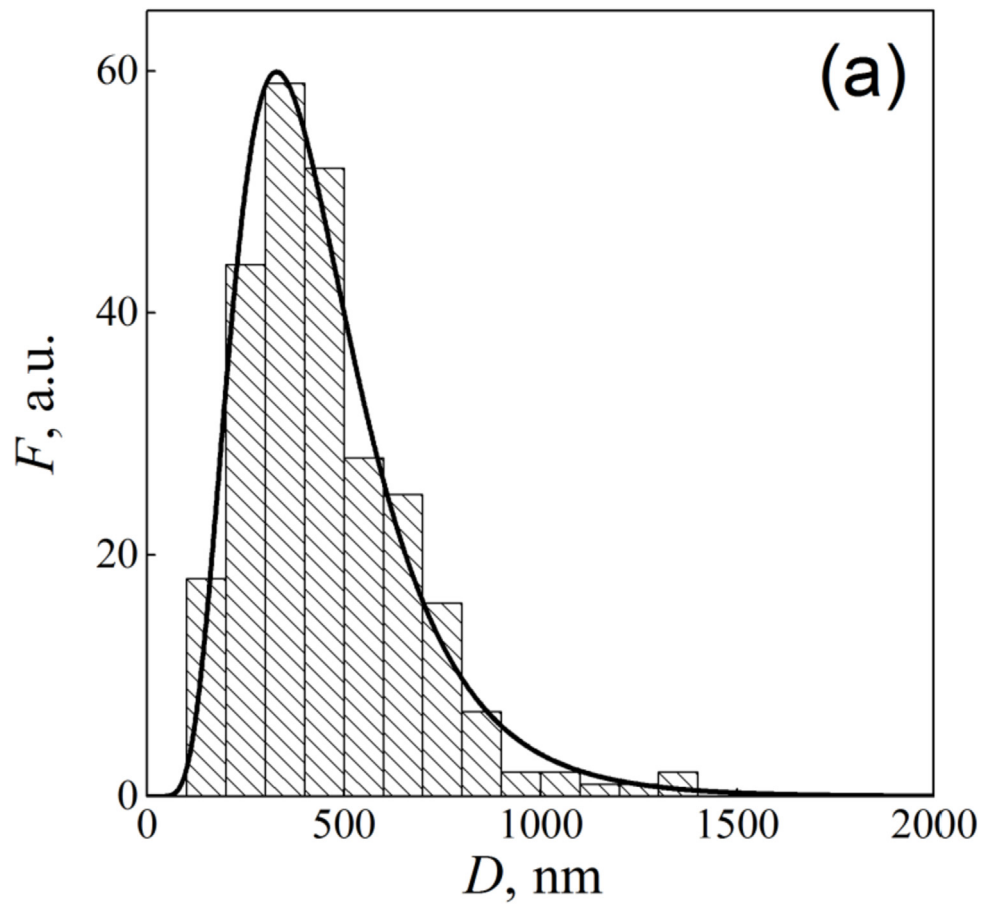

Fig. 5. The schematic of the texturing developing during the SPS process.

(caption on next page)

Fig. 7. Histograms of the grain size distribution plotted for the directions perpendicular (a) and parallel (b) to the pressing direction for. Solid lines are the fitting curves corresponding to the lognormal unimodal distribution.
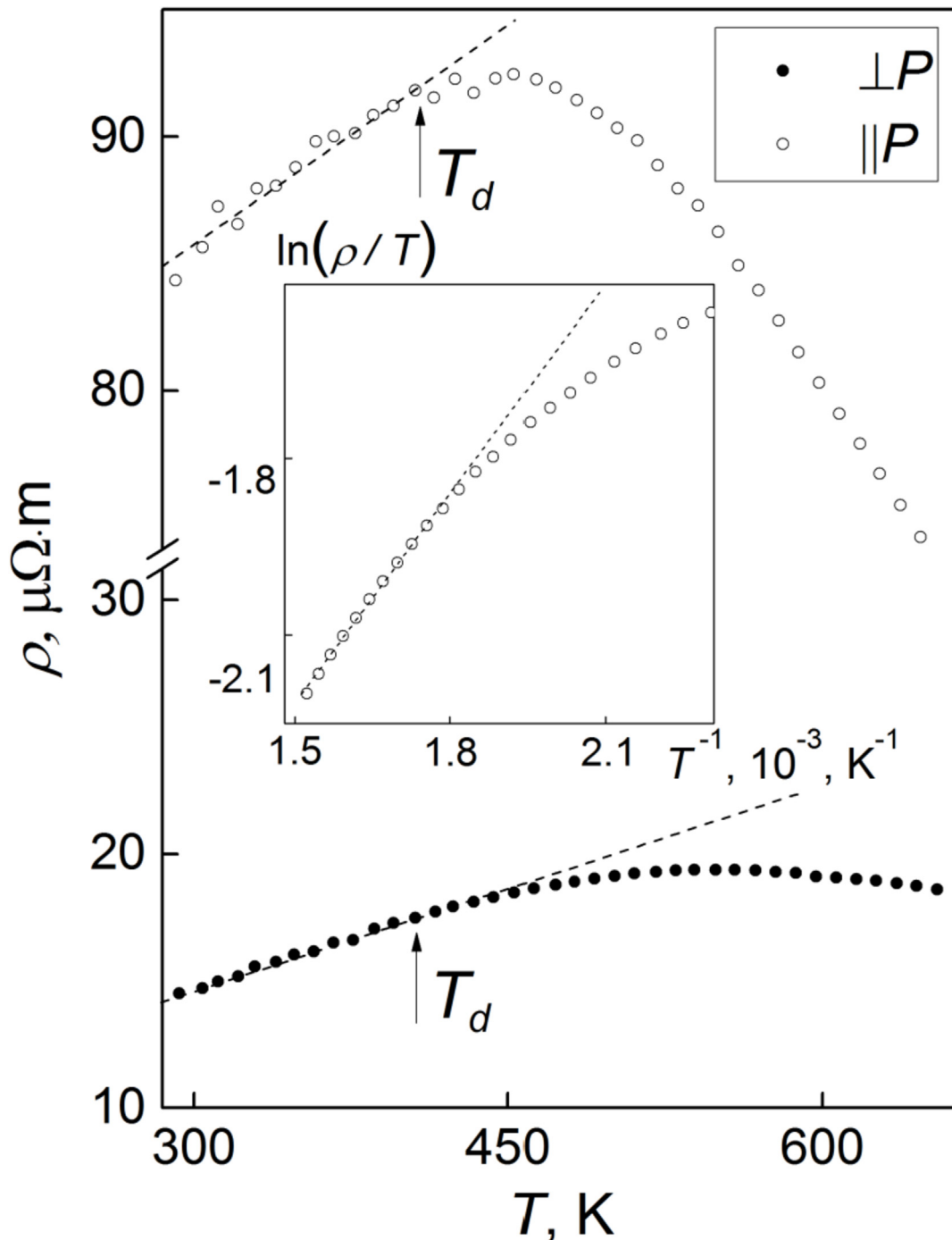

Fig. 8. The ρ vs. T dependences measured for the parallel and perpendicular orientations. Inset: the $\ln(\rho/T)$ vs. T^{-1} dependence for the parallel measurement orientation.

Starting from room temperature and up to some temperature T_d equal to ~410 K for both parallel and perpendicular orientations, ρ linearly increases with increasing temperature. This behavior is characteristic for metals and degenerate semiconductors. Above T_d, both ρ(T) dependences start to deviate downwards from linear T-dependence demonstrating a transition to semiconductor behavior. So, T_d is the temperature corresponding to conductivity mechanism change.

It is known [22] that the specific electrical resistivity of the donor semiconductors can be expressed as

$$\rho = \frac{1}{e\mu n},$$

(4)

where μ is the electron mobility.

Generally, both $n(T)$ and $\mu(T)$ changes can effect on the electrical resistivity of solids. According to Fig. 8, the $Bi_{1.9}Lu_{0.1}Te_{2.7}Se_{0.3}$ compound behaves as degenerate semiconductor from room temperature up to T_d. The degenerate semiconductors are characterized by the practically T-independent concentration of the carriers like normal metals,

that is the $\rho(T)$ change in Fig. 8 should attribute to only $\mu(T)$ changes. The T-linear growth of ρ with increasing temperature can be related to the carries scattering by phonons. Above the Debye temperature, a number of phonons increase with T and, hence, ρ increases, too. The Debye temperature for Bi_2Te_3 is equal to 155 K. So, linear T-dependences of ρ measured from room temperature up to T_d and presented in Fig. 8 are expected behavior.

To characterize a rate of T-linear $\rho(T)$ growth, the $d\rho/dT$ derivatives were calculated. These derivatives were equal to $\sim 5.7 \cdot 10^{-2}\,\mu\Omega\cdot m\cdot K^{-1}$ and $\sim 2.7\,\mu\Omega\cdot m\cdot K^{-1}$ for the parallel and perpendicular orientations, respectively. According to Ref. [23], the value of the $d\rho/dT$ derivative is related to the transport electron-phonon coupling constant, λ_{tr}, by expression

$$\lambda_{tr} = \frac{\hbar\omega_P^2}{8\pi^2 k_B} \cdot \frac{d\rho}{dT}, \tag{5}$$

where $\hbar$ is the reduced Plank constant, k_B is the Boltzmann constant and ω_p is the plasma frequency of electrons.

In this case, the big difference in the $d\rho/dT$ values found for the parallel and perpendicular orientations can be originated from various λ_{tr} values due to crystal structure anisotropy of the Bi_2Te_3-based alloys. As was mentioned above, this anisotropy resulting from the combination of various types of bonding between atoms within the layer and between the layers in the layered Bi_2Te_3 structure leads to appearance of difference in the transport properties also measured within the layer and between the layers. This difference is completely masked in non-textured grained material and gradually arises at the texture developing.

In turn, the various λ_{tr} values found for the parallel and perpendicular orientations will be reflected in the carrier mobility change. The Hall Effect was examined to determine the type, concentration and Hall mobility of the majority charge carriers. The dependences of Hall voltage drop, V_H, versus magnetic field, B, taken for the parallel and perpendicular orientations at room temperature are shown in Fig. 9. Both dependences are linear and a slope of these lines allows estimating the Hall constant, R_H.

The R_H value is equal to $\sim -0.18\,cm^3\cdot C^{-1}$. Since the majority charge carriers in compound studied are electrons, R_H has a negative sign. Taking into account a link between R_H and n expressed as $R_H = 1/(n\cdot e)$ [4], the electron concentration was also estimated as $n \approx 4.1 \cdot 10^{19}\,cm^{-3}$. Naturally, this concentration is the same for both parallel and perpendicular orientations. Finally, the Hall mobility of electrons was estimated by using a ratio $\mu_H = (R_H/\rho)$. At room temperature, μ_H was equal to $\sim 21\,cm^2\cdot V^{-1}\cdot s^{-1}$ and $\sim 123\,cm^2\cdot V^{-1}\cdot s^{-1}$ for the parallel and perpendicular orientations, respectively. So, μ_H happens to be remarkably anisotropic with room temperature anisotropy coefficient $\mu_{H\perp}//\mu_{H\|} \approx 5.85$. This anisotropy results from the textured structure forming at SPS process.

Let us discuss the $\rho(T)$ behavior above the temperature T_d, dividing whole $\rho(T)$ dependence into the low-temperature metallic conductivity (below T_d) and the high-temperature semiconductor conductivity (above T_d). A deviation the experimental $\rho(T)$ dependence from linear one above T_d can be reasonably attributed to onset of intrinsic conductivity. In this case, a thermal excitation of the charge carriers from valence band to conduction band will generate both electrons in conduction band and holes in valence band that results in the ρ decrease in accordance with expression (4). The $n(T)$ change due to the intrinsic conductivity obeys expression [24].

$$n \sim exp\left(\frac{E_g}{2k_B T}\right), \tag{6}$$

where E_g is the band gap, that is the difference between the energy at the top of the valence band the energy at the bottom of the conduction band.

Thus, in accordance with expression (4), total temperature

dependence of ρ above T_d will be determined by the temperature dependence both of the carrier mobility (T-linear growth of ρ) and the carrier concentration (T-exponential decay of ρ), that is $\rho \sim T\cdot exp[E_g/(2k_BT)]$. If such kind of the $\rho(T)$ dependence really occurs, then the ln $[\rho(T)/T]$ versus $1/T$ dependence should be linear one. Inset to Fig. 8 shows the $\rho(T)$ dependence measured for the parallel orientation and replotted in the $ln[\rho(T)/T]$ versus $1/T$ coordinates. For these coordinates at high temperatures, experimental $\rho(T)$ dependence really obeys linear law. A slope of the fitting line in inset allows estimating the band gap, which happens equal to ~ 0.21 eV. This estimate is in very well agreement with other data [1,2]. As was mentioned above, the $\rho(T)$ dependence for the perpendicular orientation is much less pronounced as compared to that for the parallel orientation and, so, it is not very well suitable to correctly estimate E_g. But, E_g like n should be independent on the measurement orientation.

3.3. The texturing effect on the seebeck coefficient

The temperature dependences of the Seebeck coefficient for the parallel and perpendicular orientations are shown in Fig. 10 (a). A sign of S is negative additionally confirming the n-type conductivity of compound studied. As was mentioned above, the Seebeck coefficient in Bi_2Te_3 and Bi_2Te_3-based alloys is a weakly anisotropic quantity. Therefore, the $S(T)$ curves for both measurement orientations lie very close to each other. The $S(T)$ curves have maximum typical for the doped Bi_2Te_3 and Bi_2Te_3-based compounds [16–20] and originated from a bipolar effect, when two types of the charge carriers are present. These maxima are centered close to temperature T_d found in the $\rho(T)$ curves (Fig. 8). As a rule, thermal excitation of the charge carries induced by the intrinsic conductivity does not change the majority carrier concentration too much, but increases the minority carrier concentration. The Seebeck coefficient for electron conductivity is negative, whereas hole conductivity is characterized by the positive Seebeck coefficient. Competition of these two contributions with opposite S signs will form the $S(T)$ maximum in Fig. 10 (a).

The temperature dependence of the Seebeck coefficient can be also used to estimate the band gap as the bipolar conductivity takes place [25]. In accordance with the Goldsmid-Sharp expression [25], the band gap (E_g), the maximum value of the Seebeck coefficient ($|S|_{max}$) and the temperature at which it occurs (T_{max}), are related by $E_g = 2e\,|S|_{max} T_{max}$. By using the experimental data $|S|_{max} \approx 170\,\mu V/K$ and $T_{max} = T_d \approx 410$ K, the Goldsmid-Sharp expression results in the E_g estimate equal to ~ 0.14 eV. This estimate is a quite different from the E_g estimate extracted from analysis of the $\rho(T)$ dependence, and, hence, much smaller the values known for $Bi_2Te_{2.7}Se_{0.3}$ [1,2]. To account for this significant deviation in the E_g value estimated by two different approaches, a validity of the Goldsmid-Sharp expression for the $Bi_2Te_{2.7}Se_{0.3}$ compound should be analyzed. According to Ref. [26], the Goldsmid-Sharp expression is invalid when either the majority-to-minority weighted mobility ratio becomes very different from 1.0 or as the band gap becomes significantly smaller than $10k_BT$. In the case of narrow gaps ($E_g \leq 6\,k_BT$), the Maxwell-Boltzmann statistic applied by Goldsmid-Sharp breaks down and the Fermi-Dirac statistic is already required. A product of $6k_BT_d$ is equal to ~ 0.21 eV, that coincides with correct E_g estimate for $Bi_2Te_{2.7}Se_{0.3}$ (also equal ~ 0.21 eV). Thus, the sample studied behaves as narrow-gap semiconductor for which the Goldsmith-Sharp expression cannot be correctly applied to estimate the band gap.

It is known [4] that the Seebeck coefficient of the degenerate semiconductors can be expressed as

$$S = \frac{2k_B^2 Tm^*}{3e\hbar^2}\left(\frac{\pi}{3n}\right)^{2/3}, \tag{7}$$

where m^* is the density-of-states effective mass of electrons.

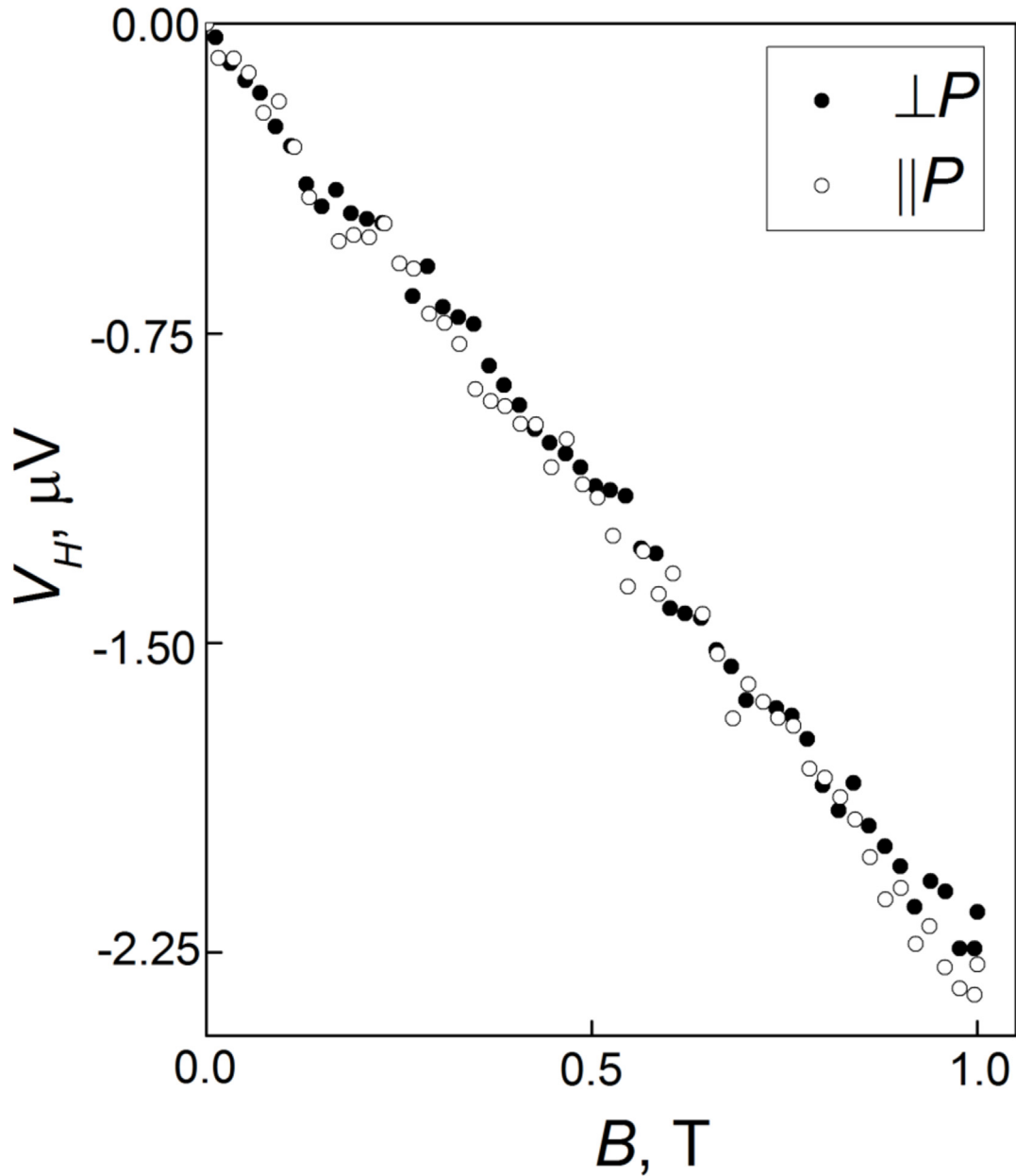In accordance with expression (7), S linearly increases as T

Fig. 9. The V_H vs. B dependences measured for the parallel and perpendicular orientations.

increases. As shown by dashed lines in Fig. 10 (a), such kind of linear T-dependences of S are really observed for initial temperatures from 290 K up to ~370 K. A rate of the linear $S(T)$ growth can be determined by the ΔS [μV/K]/ΔT [K] coefficient equal to ~0.175 and ~0.160 for the parallel and perpendicular orientations, respectively. Next, using the n and $\Delta S/\Delta T$ values, the density-of-states effective mass of electrons were estimated as ~$0.33 m_0$ (the parallel orientation) and ~$0.27 m_0$ (the perpendicular orientation), where m_0 is mass of free electron.

The temperature dependences of the power factor, S^2/ρ, are presented in Fig. 10 (b). These dependences combine the ρ and S contributions. Although the S values for the parallel and perpendicular orientations are very close to each other, the S^2/ρ values are quite different due to much higher electrical resistivity for the parallel orientation as compared to that for the perpendicular orientation.

3.4. The texturing effect on the thermal conductivity

The temperature dependences of the total thermal conductivity are

shown in Fig. 11 (a). First, k is much higher for the perpendicular orientation as compared to that for the parallel orientation. Second, both $k(T)$ curves have minima near T_d. These minima can be related to the thermal conductivity mechanism change. The lattice (or phonon) thermal conductivity, k_p, the electronic thermal conductivity, k_e, and the bipolar thermal conductivity, k_b, should be taken into account to describe the thermal conductivity in this case.

It is known [27] that the electronic thermal conductivity is related to the specific electrical conductivity, $\sigma = 1/\rho$, through the Wiedemann-Franz law

$$k_e = L\sigma T, \qquad (8)$$

where L is a constant called as the Lorenz number.

The Wiedemann-Franz law was originally developed for metals, for those the Lorenz number is equal to 2.45×10^{-8} WΩ·K^{-2}. Nevertheless, although the sample studied behaves as a degenerate semiconductor, let us use the Wiedemann-Franz law to determine the electronic thermal conductivity. Fig. 11 (b) shows the $k_e(T)$ contributions to the total
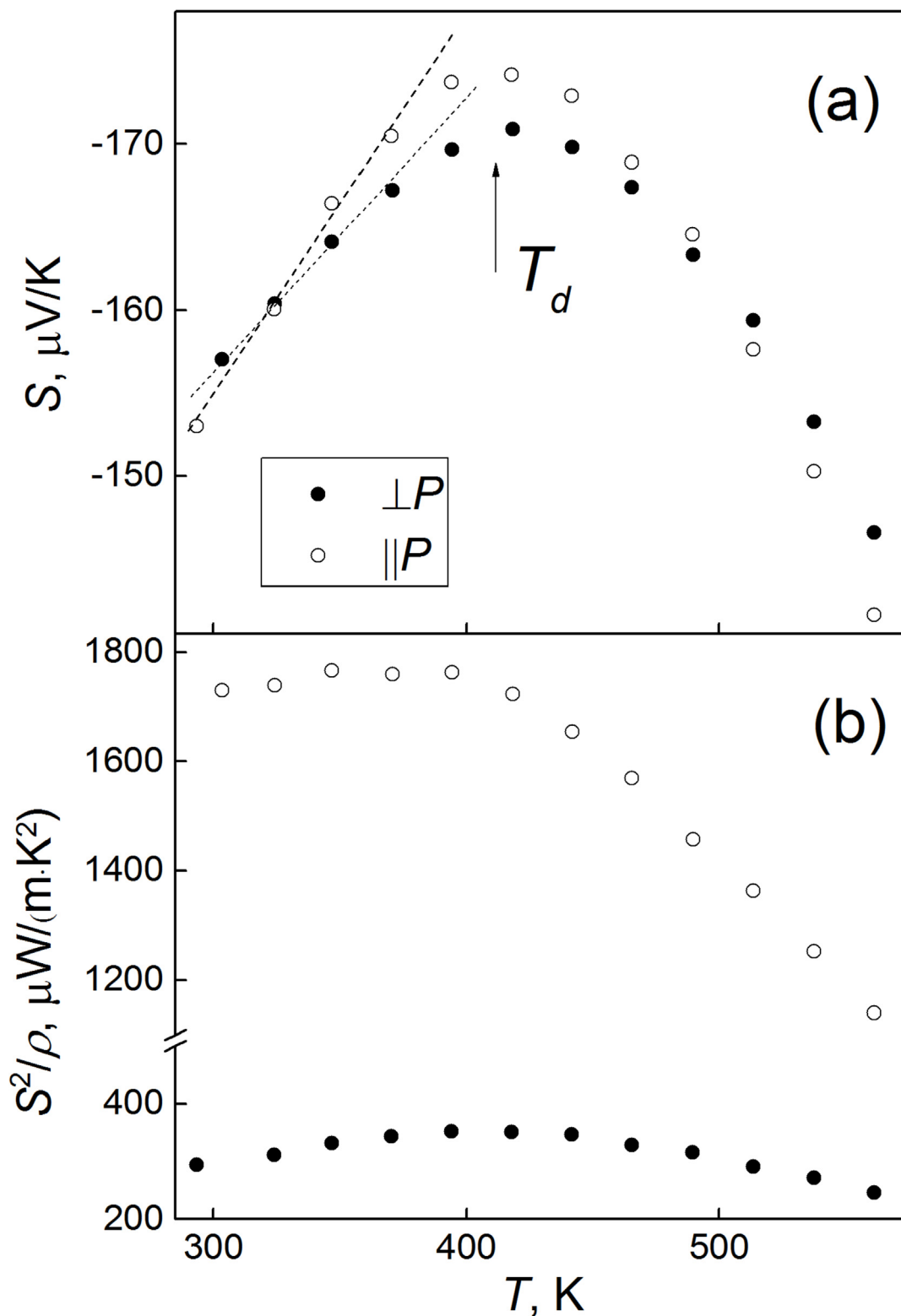
Fig. 10. The S vs. T (a) and S^2/ρ vs. T (b) dependences measured for the parallel and perpendicular orientations.

thermal conductivity. Due to lower electrical resistivity, the $k_e(T)$ contribution is much more for the perpendicular orientation. This contribution is about 40% of the total thermal conductivity, while for the parallel orientation it is equal to ~10%.

It should be noted that the value of the Lorenz number used to extract the electronic thermal conductivity can be incorrect for the semiconductors, since this value is dependent on the Fermi level

position. To correctly determine the Lorenz number, a single parabolic band model should be better applied. However, the electronic thermal conductivity was derived just to demonstrate the texturing effect on various contributions to the total thermal conductivity. In this case, the changes of these contributions for the parallel and perpendicular orientations are more important as compared to absolute values of various contributions, which are dependent on correct value of the Lorentz
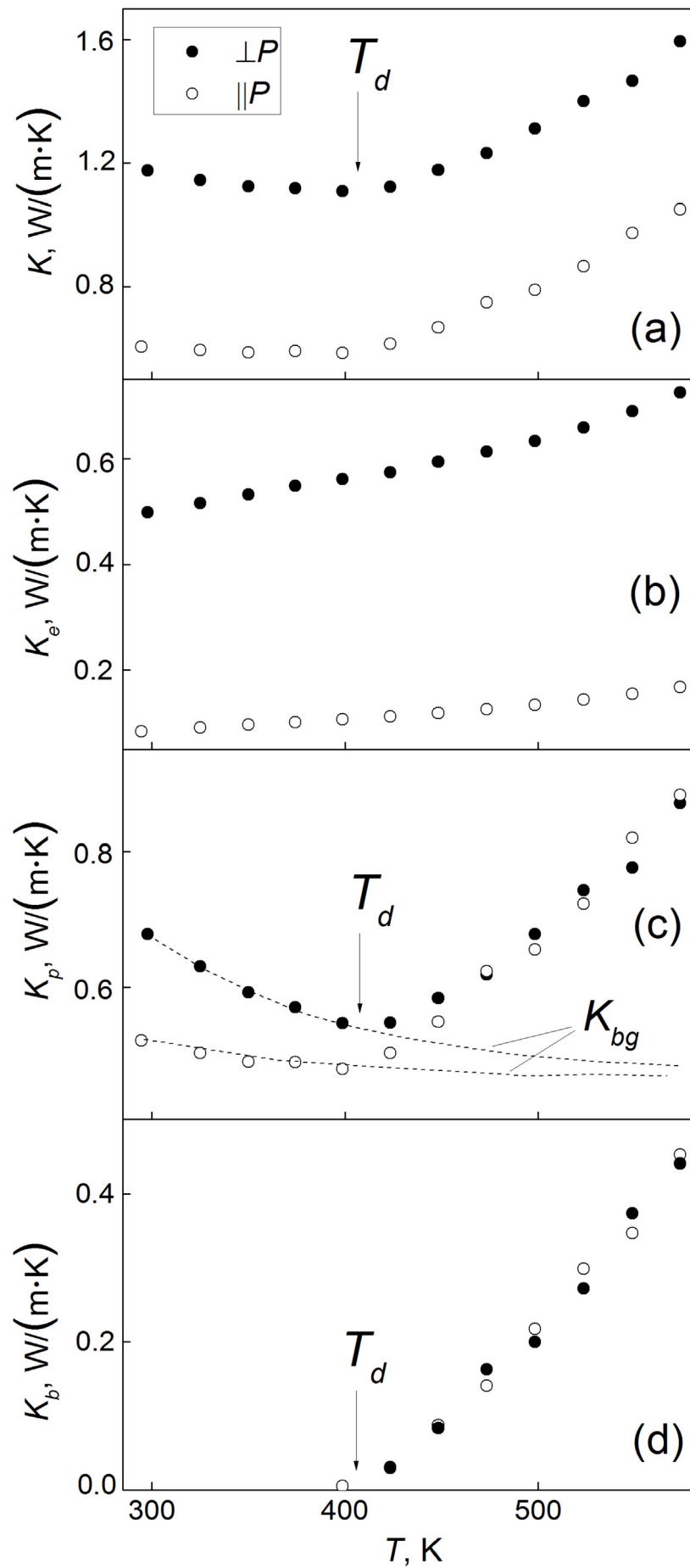
(caption on next page)

number. Moreover, the value of the electronic contribution to the total thermal conductivity estimated above (Fig. 11 (b)) is physically reasonable. So, the value of the Lorenz number applied us to extract the electronic thermal conductivity for the $Bi_{1.9}Lu_{0.1}Te_{2.7}Se_{0.3}$ can be believed to be close enough to its correct value.

The lattice contribution to the total thermal conductivity was further extracted as $k_p(T) = k(T) - k_e(T)$ (Fig. 11 (c)). Both $k_p(T)$ curves measured for the parallel and perpendicular orientations have minima at temperature corresponding T_d. Again, for low temperatures, k_p decreases with increasing temperature and the $k_p(T)$ contribution is more for the perpendicular orientation, but a difference between the k_p values for the parallel and perpendicular orientations is much less as compared to that for the k_e contribution. Above T_d, the lattice contribution already increases as temperature increases, and the $k_p(T)$ curves for both measurement orientations practically coincide. The bipolar thermal conductivity will additionally contribute in this case. To extract the bipolar thermal conductivity contribution, the $k_p(T)$ law must be defined.

It is known [28] that at high temperatures above the Debye temperature, the lattice thermal conductivity usually decreases with increasing temperature as T^{-1}. This is because the phonon specific heat is a constant at high temperatures in accordance with the Pettit-Delong law, and phonon energy increases linearly with temperature, i.e. the number of phonons increases linearly with temperature. Since the scattering rate is proportional to the number of phonons, the thermal conductivity decreases with increasing temperature. It was found that above T_d the experimental $k_p(T)$ dependence really obeys the $k_p \sim T^{-1}$ law. Then, the $k_b(T)$ contribution can be recovered by subtracting the phonon $k_{bg} \sim T^{-1}$ background (the dashed lines in Fig. 11 (c)) from the experimental $k_p(T)$ curve above T_d. When the bipolar thermal conductivity takes place, the electron-hole pairs are thermally excited at hot-side of sample due to the intrinsic conductivity process [29]. Then, these pairs as neutral formations move to cold-side. Finally, the electron-hole pairs disappear due to a recombination process. The energy of recombination per one electron-hole pair equal or greater than the band gap will be emerged as a photon. The $k_b(T)$ contributions for both measurement orientations are the same (Fig. 11 (d)), since the texturing has no effect on the intrinsic conductivity process.

3.5. The texturing effect on the thermoelectric figure-on-merit

Finally, the ρ, S and k values were used to plot the $ZT(T)$ dependences for the parallel and perpendicular orientations (Fig. 12).

At texturing, the specific electrical resistivity (Fig. 8) increases and the total thermal conductivity (Fig. 11) decreases for the parallel orientation as compared to these properties for the perpendicular orientation. The Seebeck coefficients for both orientations are almost equal. The increase of the electrical resistivity is stronger than the decrease of the thermal conductivity resulting in almost three-fold enhancement of ZT for the perpendicular measurement orientation. It should be again mentioned that for the parallel orientation the thermoelectric properties are preferentially measured along c-axis of the grains, while for the parallel orientation these properties are measured within the a-b plane.

Finally, let us discuss the texture anisotropy in the specific electrical resistivity and the total thermal conductivity of $Bi_{1.9}Lu_{0.1}Te_{2.7}Se_{0.3}$ reported above. Fig. 13 shows the temperature dependences of the anisotropy coefficients, $\rho(\|P)/\rho(\bot P)$ and $k(\|P)/k(\bot P)$.

First of all, the $\rho(\|P)/\rho(\bot P)$ ratio seems to be too big. For instance, this anisotropy coefficient is equal to ~ 5.85 at room temperature. Really, it is even a bit more than the ρ_c/ρ_{ab} value for the Bi_2Te_3 and Bi_2Te_3-based single crystals [7–9]. For textured samples so high anisotropy in the electrical properties could be expected only for ideally

oriented sample with the orientation factor $f = 1$. The sample studied in our work had $f \approx 0.38$. Moreover, the ideally oriented sample cannot be prepared by SPS method. Typical $\rho(\|P)/\rho(\bot P)$ values known from literature for the textured alloys based on Bi_2Te_3 are ~ 1.7 [8], ~ 1.8 [9], ~ 2.5 [10], $\sim 2 \div 2.4$ [13], ~ 1.35 [14] and [15]. Obviously, the $\rho(\|P)/\rho(\bot P)$ ratio obtained for the textured $Bi_{1.9}Lu_{0.1}Te_{2.7}Se_{0.3}$ is the highest ratio by now. Increase of the crystal structure anisotropy typical for the Bi_2Te_3-based alloys and arising from the SPS texturing cannot be applied to account for so big $\rho(\|P)/\rho(\bot P)$ ratio observed in our experiment. Hence, other mechanisms should be taken into account, too.

Additional scattering by the grain boundaries resulting in decrease of the carrier mobility could be considered as one of such reasonable mechanisms. This mechanism is effective for micro- and nanostructural materials [28,30,31]. The average grain size for the textured $Bi_{1.9}Lu_{0.1}Te_{2.7}Se_{0.3}$ was found to be very different for directions parallel (~ 50 nm, Fig. 7 (b)) and perpendicular (~ 400 nm, Fig. 7 (a)) to the pressing direction. So, more number of the grain boundaries acting as the scattering centers exist for the parallel orientation and then for this orientation the grain boundary scattering should be really more effective.

Effect of the grain boundaries on the electrical resistivity can be taken into account in frames of the Mayadas-Shatzkes model [32]. According to this model, the grain boundaries can be regarded as potential barriers which have to be overcome by the electrons. The scattering electron processes from the potential barriers will result in decreasing of the electron mobility, and hence, in higher specific electrical resistivity. A relation between the electron mobility due to the grain boundaries scattering, μ_{GB}, and the electron mobility of the grainless materials, μ_{cryst}, can be expresses as [33].

$$\frac{\mu_{GB}}{\mu_{cryst}} \approx \frac{1}{1 + 1.34\left(\frac{R}{1-R}\right)\frac{l_e}{\overline{D}}}, \tag{9}$$

where R is the reflectivity of the grain boundaries, l_e is the electron mean free path and $\overline{D}$ is the average grain size.

The mobility μ_{cryst} determines the bulk resistivity characteristic for the resistivity of grain material, while the mobility μ_{GB} results in additional resistivity contribution due to the grain boundaries.

In accordance with expression (9), decreasing in $\overline{D}$ should result in decreasing in μ_{GB}, and hence, in increasing in the specific electrical resistivity (in accordance with expression (4)).

Thus, there are two contributions at least to the specific electrical resistivity measured between room temperature ant the temperature $T_d \approx 410$ K (Fig. 8). For these temperatures, the $Bi_{1.9}Lu_{0.1}Te_{2.7}Se_{0.3}$ sample studied behaves as degenerate semiconductor that is characterized by the T-independent concentration of the carriers like normal metals. As mentioned above, the first of these contributions resulting in T-linear growth of ρ with increasing temperature should be attributed to the carries scattering by phonons. The second contribution considered above could be related to the grain boundary scattering of the electrons. Since T-linear growth of ρ is mainly due to the phonon scattering, the grain boundary scattering should be believed to be practically T-independent, that is contribution of the grain boundary scattering can be although big enough, but constant contribution to the total electrical resistivity within the temperature range discussed.

Besides the electron scattering, the phonon scattering by the grain boundaries can also take place. Since the $k(\|P)/k(\bot P)$ coefficient is, firstly, much less than the $\rho(\|P)/\rho(\bot P)$ coefficient and, secondly, its value is in better agreement with literature data, the boundary scattering weakly contributes to the total thermal conductivity. That is the texturing effect on k can be mainly explained as recovery of the crystal structure anisotropy typical for the Bi_2Te_3-based alloys. Difference in the free paths for electron and phonon can result in various texturing
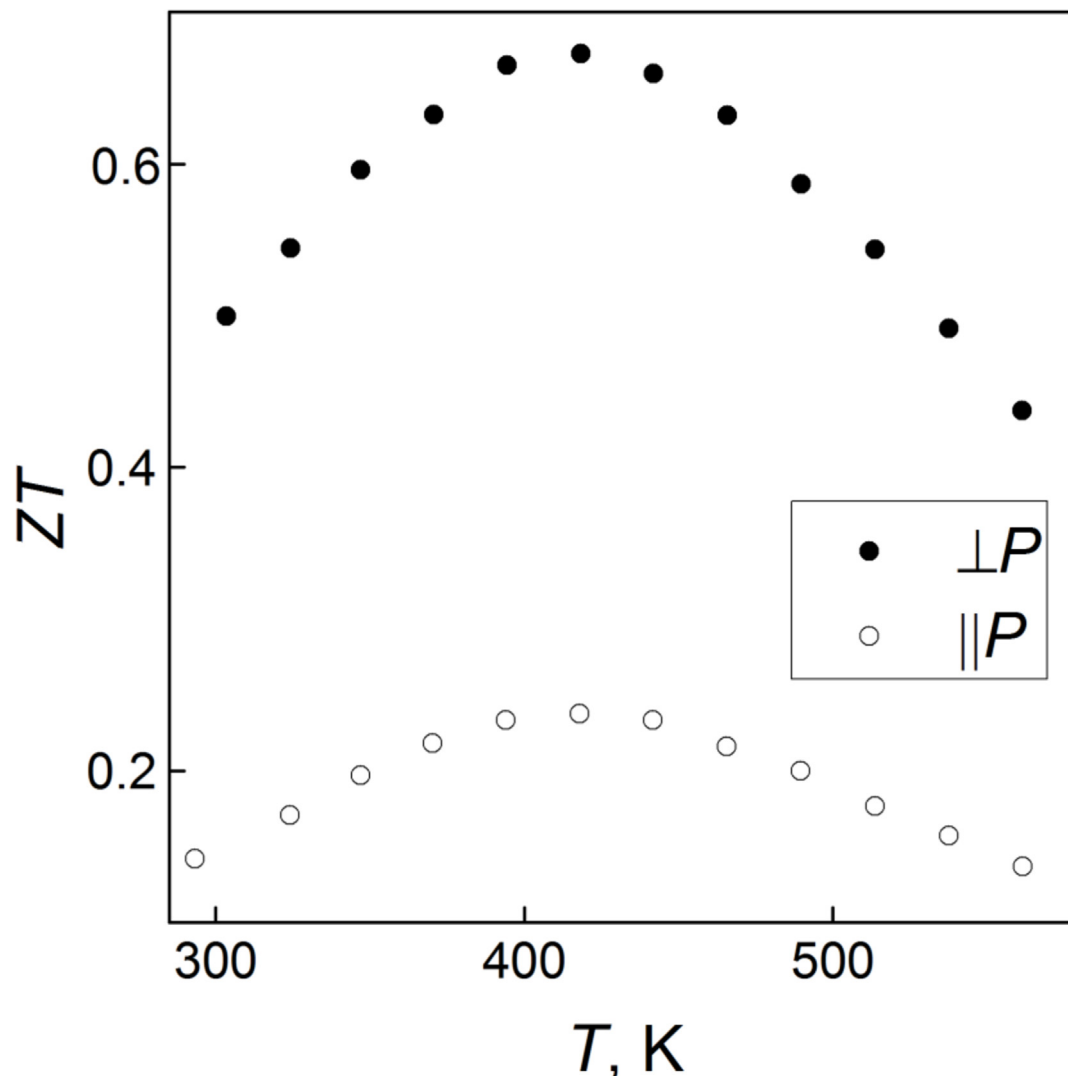
Fig. 12. The *ZT* vs. *T* dependences measured for the parallel and perpendicular orientations.

effect on the specific electrical resistivity and the thermal conductivity [28,30,31].

Another feature in the anisotropy coefficients for the specific electrical resistivity and the total thermal conductivity (Fig. 13) is their strong enough temperature dependence. Really, both coefficients decrease with increasing temperature. This behavior can be related to a gradual decrease of the crystal structure anisotropy as temperature increases. Indeed, there is some difference in linear thermal expansion coefficients of bismuth telluride taken along the principal crystallographic α_c and α_a axes [34]. Perhaps, this difference could be attributed to the temperature change of crystal structure anisotropy. Further experiments should be done to account for the temperature dependence of the $\rho(\|P)/\rho(\perp P)$ and $k(\|P)/k(\perp P)$ coefficients.

4. Conclusion

Thus, the textured *n*-type $Bi_{1.9}Lu_{0.1}Te_{2.7}Se_{0.3}$ samples were prepared by spark plasma sintering. The texture developing in the 001 direction parallel to the SPS pressing direction was confirmed by X-ray diffraction analysis and scanning electron microscopy. The textured samples are characterized by grain lamellar structure forming. The lamellar sheets lie in plane perpendicular to the pressing direction. The average grain size measured along the pressing direction (~ 50 nm) is much less as compared to the average grain size measured in the perpendicular

direction against (~ 400 nm). A strong anisotropy in the specific electrical resistivity and the total thermal conductivity was found at measurements along directions parallel and perpendicular to the pressing direction. This anisotropy is originated from partial recovery of crystal structure anisotropy typical for the single crystal Bi_2Te_3-based alloys. Besides, the grain boundary scattering of electrons can additionally effect on the electrical properties anisotropy. Within the $290 \div 650$ K interval, the specific electrical resistivity increases and the total thermal conductivity decreases for parallel orientation as compared to these properties for the perpendicular orientation, while the Seebeck coefficient for both orientations is almost equal. Combination of these quantities results in almost three-fold enhancement of the thermoelectric figure-of-merit coefficient for the perpendicular measurement orientation (~ 0.68 against ~ 0.24 at ~ 420 K).
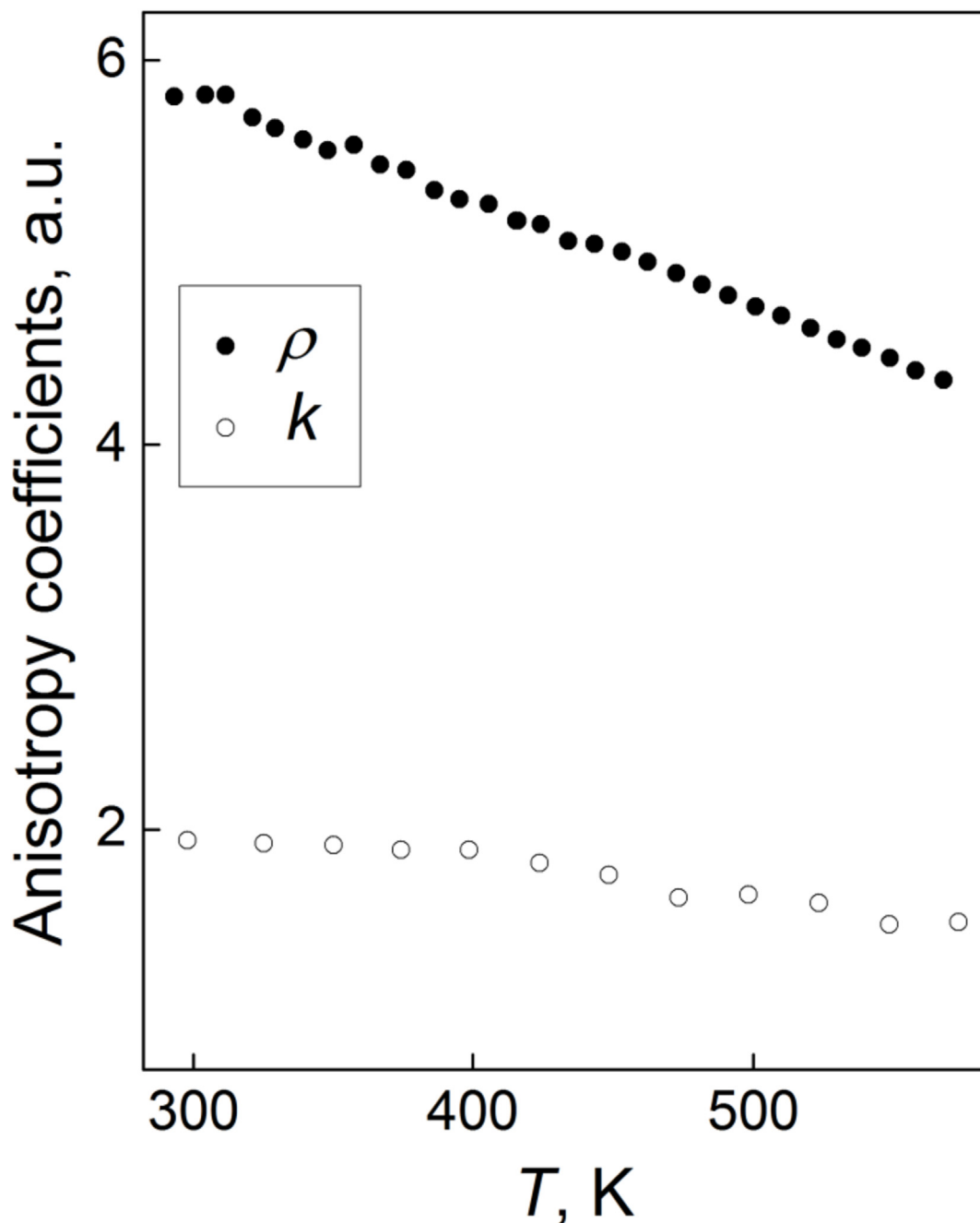
Declarations of interest

None.

Acknowledgements

Fig. 13. The temperature effect on anisotropy in the specific electrical resistivity and the total thermal conductivity.

References

[1] H.J. Goldsmid, Bismuth telluride and its alloys as materials for thermoelectric generation, Materials 7 (2014) 2577–2592.

[2] H. Scherrer, S. Scherrer, Thermoelectric properties of bismuth antimony telluride solid solutions, in: D.M. Rowe (Ed.), Thermoelectrics Handbook: Macro to Nano, CRC Taylor and Francis, Boca Raton, FL, USA, 2012.

[3] P. Zou, G. Xu, S. Wang, P. Chen, F. Huang, Effect on high pressure sintering and annealing on microstructure and thermoelectric properties of nanocrystalline $Bi_2Te_{2.7}Se_{0.3}$ doped with Gd, Progress in Natural Science, Mater. Int. 24 (2014) 210–217.

[4] K.C. Lukas, W.C. Liu, Z.F. Ren, C.P. Opeil, Transport properties of Ni, Co, Fe, Mn doped $Cu_{0.01}Bi_2Te_{2.7}Se_{0.3}$ for thermoelectric device applications, J. Appl. Phys. 112 (2012) 054509–1-5.

[5] H. Scherrer, S. Scherrer, Bismuth telluride, antimony telluride and their solid solutions, in: D.M. Rowe (Ed.), CRC Handbook of Thermoelectrics, CRC Press, Boca Raton, FL, USA, 1995.

[6] T. Caillat, M. Carle, P. Pierrat, H. Scherrer, S. Scherrer, Thermoelectric properties of $(Bi_xSb_{1-x})_2Te_3$ single crystal solid solutions grown by the T.H.M. method, J. Phys. Chem. Solid. 53 (1992) 1121–1129.

[7] G.S. Nolas, J. Sharp, H.J. Goldsmid, Thermoelectrics Basic Principles and New Materials Developments, Springer, Berlin, 2001.

[8] O. Ben-Yehuda, R. Shuker, Y. Gelbstein, Z. Dashevsky, M.P. Dariel, Highly textured Bi_2Te_3-based materials for thermoelectric energy conversion, J. Appl. Phys. 101 (2007) 113707–1-6.

[9] J.J. Shen, L.P. Hu, T.J. Zhu, X.B. Zhao, The texture related anisotropy of thermoelectric properties in bismuth telluride based polycrystalline alloys, Appl. Phys. Lett. 99 (2011) 124102–1-3.

[10] X. Yan, B. Poudel, W.S. Liu, G. Joshi, H. Wang, Y. Lan, D. Wang, G. Chen, Z.F. Ren, Experimental studied on anisotropic thermoelectric properties and structures of n-type $Bi_2Te_{2.7}Se_{0.3}$, Nano Lett. 10 (2010) 3373–3378.

[11] S.D. Bhame, D. Pravarthana, W. Prellier, J.G. Noudem, Enhanced thermoelectric performance in spark plasma textured bulk n-type $Bi_2Te_{2.7}Se_{0.3}$ and p-type $Bi_{0.5}Sb_{1.5}Te_3$, Appl. Phys. Lett. 102 (2013) 2190–2191-3.

[12] X.A. Fan, J.Y. Yang, R.G. Chen, H.S. Yun, W. Zhu, S.Q. Bao, X.K. Duan,

Characterization and thermoelectric properties of p-type 25%Bi$_2$Te$_3$–75%Sb$_2$Te$_3$ prepared via mechanical alloying and plasma activated sintering, J. Phys. D Appl. Phys. 39 (2006) 740–745.

[13] J. Jiang, L. Chen, S. Bai, Q. Yao, Q. Wang, Fabrication and thermoelectric performance of textured n-type Bi$_2$(Te,Se)$_3$ by spark plasma sintering, Mater. Sci. Eng. B 117 (2005) 334–338.

[14] Q. Lognon, F. Gascoin, O.I. Lebedev, L. Lutterotti, S. Gascoin, D. Chateigner, Quantitative texture analysis of spark plasma textured n-Bi$_2$Te$_3$, J. Am. Ceram. Soc. 97 (2014) 2038–2045.

[15] J.-J. Shen, T.-J. Zhu, X.-B. Zhao, S.-N. Zhang, S.-H. Yang, Z.-Z. Yin, Recrystallization induced in situ nanostructures in bulk bismuth antimony tellurides: a simple top down route and improved thermoelectric properties, Energy Environ. Sci. 3 (2010) 1519–1523.

[16] C. Andre, D. Vasilevskiy, S. Turenne, R.A. Masut, Increase in the density of states in n-type extruded (Bi$_{(1-x)}$Sb$_x$)$_2$(Te$_{(1-y)}$Se$_y$)$_3$ thermoelectric alloys, J. Phys. D Appl. Phys. 44 (2011) 235401–1-8.

[17] F. Wu, H. Song, J. Jia, X. Hu, Thermoelectric properties of rare earth-doped n-type Bi$_2$Te$_{2.7}$Se$_{0.3}$ nanocomposites, Bull. Mater. Sci. 37 (2014) 1007–1012.

[18] F. Wu, H. Song, J.J. Jia, F. Gao, Y. Zhang, X. Hu, Thermoelectric properties of Ce-doped n-type Ce$_x$Bi$_{2-x}$Te$_{2.7}$Se$_{0.3}$ nanocomposites, Phys. Stat. Sol. A. 210 (2013) 1183–1189.

[19] J. Yang, F. Wu, Z. Zhu, L. Yao, H. Song, X. Hu, Thermoelectrical properties of lutetium-doped Bi$_2$Te$_3$ bulk samples prepared from flower-like nanopowders, J. Alloy. Comp. 619 (2015) 401–405.

[20] O. Ivanov, M. Yaprintsev, R. Lyubushkin, O. Soklakova, Enhancement of thermoelectric efficiency in Bi$_2$Te$_3$ via rare earth element doping, Scripta Mater. 146 (2018) 91–94.

[21] F.J. Humphreys, M. Hatherly, Recrystallization and Related Annealing Phenomena, Elsevier, Oxford, UK, 2004.

[22] J. Seo, K. Park, D. Lee, C. Lee, Microstructure and thermoelectric properties of p-Type Bi$_{0.5}$Sb$_{0.5}$Te$_{0.5}$ compounds fabricated by hot pressing and hot extrusion, Scripta Mater. 38 (1998) 477–484.

[23] W.A. Vareka, A. Zettl, Linear temperature dependent resistivity ant constant volume in Rb$_3$C$_{60}$, Phys. Rev. Lett. 72 (1994) 4121–4124.

[24] S. Kasap, C. Koughia, H. Ruda, R. Johanson, Handbook of Electronic and Photonic Materials, Springer, Berlin, 2006.

[25] H.J. Goldsmid, J.W. Sharp, Estimation of the thermal band gap of a semiconductor from seebeck measurements, J. Electron. Mater. 28 (1999) 869–872.

[26] Z.M. Gibbs, H.-S. Kim, H. Wang, G.J. Snyder, Band gap estimation from temperature dependent Seebeck measurement – deviations from the 2e|S|maxTmax relation, Appl. Phys. Lett. 106 (2015) 022112–1-5.

[27] W. Liu, X. Yan, G. Chen, Z. Ren, Recent advances in thermoelectric nanocomposites, Nano Energy 1 (2012) 42–56.

[28] M.D. Daybell, W.A. Steyert, Localized magnetic impurity states in metals: some experimental relationships, Rev. Mod. Phys. 40 (1968) 380–389.

[29] J.S. Blakemore, Solid State Physics, second ed., Cambridge University Press, Cambridge, 1985.

[30] A.J. Minnich, M.S. Dresselhaus, Z.F. Ren, G. Chen, Bulk nanostructured thermoelectric materials: current research and future prospects, Energy Environ. Sci. 2 (2009) 466–479.

[31] A. Bulusu, D.G. Walker, Review of electronic transport models for thermoelectric materials, Superlattice. Microst. 44 (2008) 1–36.

[32] A.V. Mayadas, M. Shatzkes, Electrical-resistivity model for polycrystalline films: the case of arbitrary reflection at external surfaces, Phys. Rev. B 1 (1970) 1382–1388.

[33] S. Riedel, J. Röber, T. Geßner, Electrical properties of copper films produced by MOCVD, Microelectron. Eng. 33 (1997) 165–172.

[34] L.M. Pavlova, YuI. Shtern, R.E. Mironov, Thermal expansion of bismuth telluride, High Temp. 49 (2011) 369–379.